2023

# Three-Dimensional Fractal Analysis of Idiopathic Pulmonary Fibrosis

William Wright

# Three-Dimensional Fractal Analysis of Idiopathic Pulmonary Fibrosis

William Wright

**Abstract**

The characterization of lung tissue architecture in Idiopathic Pulmonary Fibrosis (IPF) can provide useful insights into disease presentation and progression. In this study, we propose a novel three-dimensional (3D) fractal analysis to quantify the behavior of lung tissue in both healthy and bleomycin (BLM)-induced fibrotic mouse models. The fractal dimension (FD), which is a statistical index of complexity, was calculated for each voxel in reconstructed micro-CT images of the lung samples. These values were plotted on a kernel density estimation (KDE) plot, generating a distribution of FDs for each sample. Results indicate a slight but not statistically significant difference in average FD between the control and BLM samples. Tissue densities between the two groups were also compared in Hounsfield units (HU), a radiodensity scale, revealing elevated collagen concentrations and peripheral fibrosis in the BLM groups, consistent with IPF. Due to our small sample size of only 9 mouse lungs, further conclusions about the structural differences between healthy and fibrotic lungs are impaired. However, the results suggest disparities in the organization and/or collagen density between groups. Therefore, further assessments encompassing density features into the FD may prove to be an effective mode for differentiating and/or describing healthy and IPF lungs.

**Introduction**

Idiopathic Pulmonary Fibrosis is a chronic, progressive lung disease in which collagenous scar tissue accumulates around the alveoli in the lungs – the tiny air sacs responsible for gas exchange during breathing. With IPF, the interstitial lung tissue becomes increasingly thick and stiff, causing permanent scarring and deformation of the peripheral lung surface with subsequent propagation into other lung regions [1]. This progression induces alveolar remodeling, bronchiectasis (bronchiole dilation), and parenchymal fibrosis, ultimately impairing oxygen intake and leading to respiratory failure [1]. Hallmark signs of IPF are associated with histopathological and/or radiologic patterns of usual interstitial pneumonia (UIP), characterized by patchy, interstitial areas of collagen, honeycombing zones consisting of distinct fibrous walls and cystic airspaces, and general tissue distortion on high-resolution computed tomography (HRCT) and histopathological images [1]. The diagnosis and management of IPF remain challenging due to its unknown etiology, high treatment costs, nonspecific respiratory symptoms, and structural heterogeneity. Patients are frequently misdiagnosed or receive an indeterminate diagnosis as the morphology of IPF often resembles other lung conditions. One study reported that more than 40 percent of patients diagnosed with IPF initially received a misdiagnosis, with a mean diagnostic delay of 2.1 years [2]. Furthermore, only two FDA-approved pharmacotherapeutic agents exist on the market (nintedanib and pirfenidone), both

of which act to slow collagen deposition and fibrotic development but fail to reverse the progression of the disease [3]. The resulting prognosis remains poor, with a mean survival rate of ~2.5-5 years after a definitive diagnosis is made [4].

While the causes of IPF are unknown, studies suggest that aging, environmental factors, genetics, epigenetic reprogramming, smoking, infectious agents, gastroesophageal reflux, and abnormal immune cell activity could all be linked to IPF etiology [5]. One or more of these factors cause persistent aberrant activation of the epithelium, leading to the hyperactive secretion of a set of pro-fibrotic growth factors, chemokines, and angiostatic procoagulant mediators collectively known as senescence-associated secretory phenotype (SASP) factors [6]. SASP factors cause abnormal wound healing, in which fibroblasts and myofibroblasts in the IPF lung present a stressed and senescent phenotype, including resistance to apoptosis and exaggerated production of extracellular matrix components [6]. This induces a mechanotransducive feedback loop whereby increased matrix stiffness affects the behavior and concentration of the fibroblasts and epithelial cells, thus causing irreversible damage and fibrosis. Other fragments of the ECM, including fibrin, fibronectin, and hyaluronan, are also all potentially fibrogenic. Moreover, fibrosis progression may be self-sustaining once initiated, implying that the mechanisms behind disease initiation and progression might be uncoupled [7]. Therefore, the physical remodeling of the lung architecture is of particular interest as it is the primary feature of IPF progression and the main diagnostic indicator. In particular, honeycombing patterns and increased opacity of the lung in HRCT images, predominantly seen in the basal (bottom) and subpleural regions of the lung, are used to confirm UIP before more intrusive fluid and lung biopsy tests are performed [8]. The presence of dense fibrosis with structural distortion, patchy involvement of lung parenchyma by fibrosis, and fibroblast foci further confirm UIP in histopathology [8]. Thus, the diagnosis and characterization of disease progression currently rely on qualitative lung tissue analyses through the indication of UIP, without any standard or quantitative methods available for describing disease type and severity.

Computational and mathematical models can be utilized to better characterize the structure and mechanisms of fibrotic lung tissue development. Fractal analysis (FA) is one potential method that can be employed to achieve this goal, presenting a contemporary approach in which nontraditional mathematics is applied to patterns and entities to measure their complexity [9]. FA is not limited to biological tissue and could be used to help differentiate healthy and diseased lungs using numerical data. In this work, we propose a 3D fractal analysis applied to both healthy and fibrotic lung tissue to provide insight into disease progression and open new lines of investigation in quantitative imaging analysis applied to IPF research. It was applied to reconstructed micro-CT images of healthy and Bleomycin (BLM)-induced fibrotic mouse lungs to mimic the remodeling of lung tissue in fibrotic human lungs. The lung tissue density and fractal behavior were compared in both groups to look for quantitative-based distinctions that could be used in conjunction with standard clinical analyses of IPF. We hypothesize that thoroughly assessing the structural remodeling of the lungs during IPF might provide critical answers for understanding fibrotic development and improving disease progression analysis, diagnostics, and other future inquiries related to IPF.

**Background**

The concept of fractal geometry was introduced by Benoit Mandelbrot in 1977, to describe the complexity of natural forms. In mathematics, fractals are infinitely complex self-similar geometric patterns that repeat across different length scales. Natural forms such as snowflakes, trees, and the airway tree exhibit approximate fractal geometry and can be characterized by a non-integer value known as the fractal dimension (FD), a statistical index of complexity derived from power law functions that describe the space-filling capacity of the object. In other words, natural entities are not purely one, two, or three-dimensional, instead comprising elements that fall within multiple dimensions. FA, therefore, allows us to describe the interdimensional geometry of objects, providing quantitative values for comparing like forms such as healthy and diseased lungs.

FA is not new in the medical context, mainly being used to identify abnormalities in biological systems based on differences in relative FD. Prior studies have applied FA to the lungs and other organs; however, none have developed a 3D FA related to IPF structure. One paper outlined the use of FA for characterizing fibroblast foci in Chronic Obstructive Pulmonary Disease (COPD), examining the size distribution of emphysematous clusters to improve clinical assessments [10]. 3D low attenuation clusters were reconstructed from CT scans based on voxel thresholds, and an index similar to the FD was calculated for each case based on cluster sizes [10]. This provided information regarding the structure-function relationship of the lung in COPD, with methodologies similar to those introduced in our approach. Another study characterized the fibroblast foci in IPF using an integrated micro-CT and histology methodology, but without the use of fractal analysis [11]. The results provided visual representations of the heterogeneous lung structure seen with IPF and confirmed that foci represent discrete sites of lung injury and repair with suggestions of previously unrecognized plasticity [11]. Assessments of FD have been used to explore other models as well, including the brain. Stephan Krohn et al., evaluated the use of the 3D FD on neuroimaging datasets as a marker of structural complexity in the brain, concluding that FD estimates are reliable yet sensitive to image characteristics [12].

Calculating the FD of an object can be achieved using a variety of methods, such as box-counting, lacunarity, root mean square, and mass-radius methods. The box-counting algorithm is the most commonly employed method, as it can be applied to patterns extracted from still images, including the micro-CT scans used in our study. In the standard box-counting model, a grid of boxes of size $L$ is placed over the object and the number of boxes required to cover the object $N(L)$, is counted. The relationship between $N(L)$ and $L$ is plotted on a log-log plot, and if the relationship appears linear, the data can be fitted with a straight line where the absolute value of the negative slope of the linear regression corresponds to the FD of the object as depicted in Figure 1.

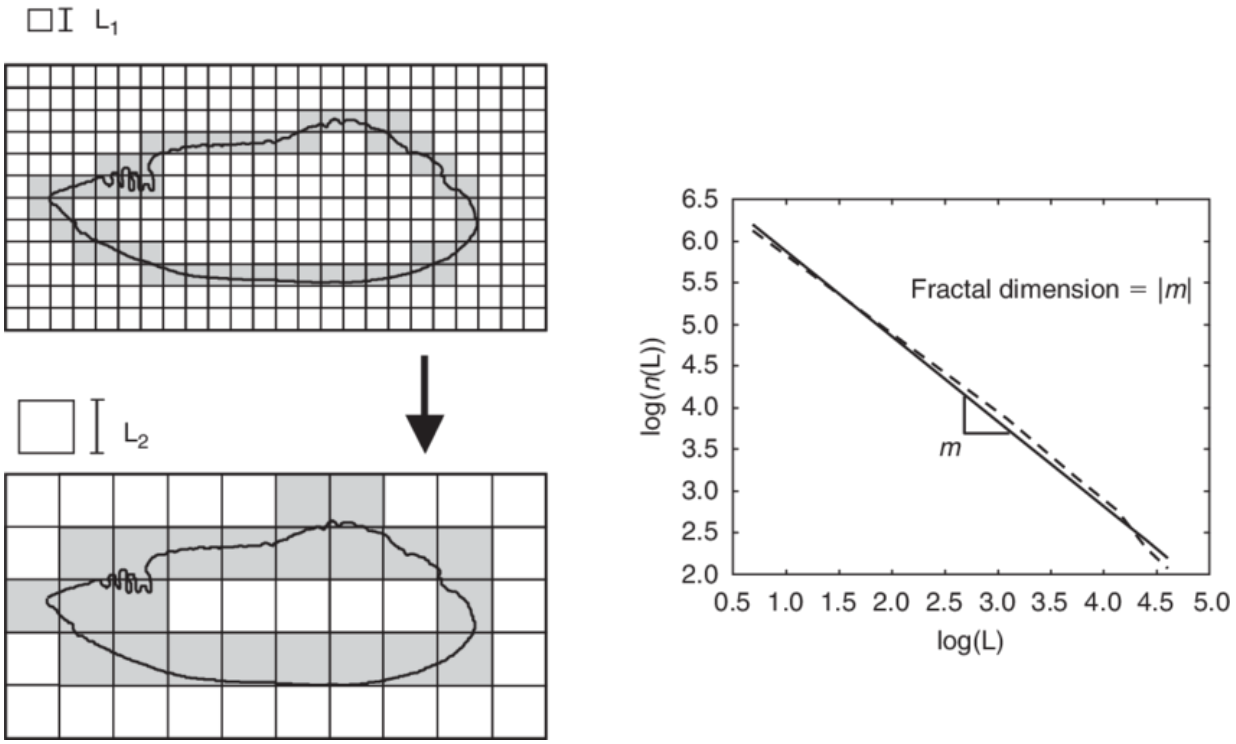


**Figure 1: Illustration of the box-counting method for estimating the fractal dimension.** Box sizes of increasing side lengths are overlayed on the image. The number of boxes required to cover the image is plotted against the corresponding box size on a log-log scale to calculate the FD [13].

The box-counting method and variations of the approach can be applied to the lung structure in IPF, as previous studies have successfully implemented it in similar biological models. However, the methods for applying fractal analysis in biology and medicine are not standardized, with studies yielding very different results due to software, imaging, and analytic disparities. Most critically, previous approaches do not account for local structures or FD distributions, gathering insight into the complexity of the model as a whole but not capturing the local differences present throughout the tissue. By using the 3D FA proposed in our study, we expect to gain a better understanding of disease characteristics through visual representations of the structural behavior in IPF and healthy lung tissue.

**Methods and Materials**

*Mouse Models*

Preclinical drug trials for treating IPF have traditionally utilized mouse models with bleomycin (BLM)-induced pulmonary fibrosis. BLM is a chemotherapeutic agent that also acts as a profibrotic agent when administered [14]. It's suggested that BLM acts by causing single and double-strand DNA breaks, leading to cell apoptosis and BLM-induced injury. This triggers a set of reactions that results in the overproduction of reactive oxygen species (ROS), ultimately

leading to fibroblast activation, ECM deposition, and the development of fibrosis [14]. While BLM mouse models are not a perfect translation to IPF in human lungs, they represent the most commonly applied experimental model for preclinical trials [14].

In this study, all animal use and treatment protocols were reviewed and approved by the Institutional Animal Care and Use Committee at the University of Vermont and the University of Colorado. Pulmonary fibrosis was induced in C57BL/6NJ mice using BLM (3U $kg^{-1}$ body weight, APP Pharmaceuticals), administered oropharyngeally as previously described (Aesif et al. 2009; Anathy et al. 2012.) [15],[16]. Eight-week-old mice were treated with bleomycin, while an aged-matched group received phosphate-buffered saline (PBS) as a control [17]. The lungs from mice instilled with BLM were housed for three weeks before being fixated and harvested. The samples were air-inflated at a 5 cmH2O positive-ended expiratory pressure (PEEP) and perfused with fixative at a constant pressure of 25 cm H2O [17]. Before imaging, the lungs were contrasted with uranyl acetate/osmium tetroxide and embedded in glycol methacrylate [17]. Five BLM (*n = 5*) and four (*n = 4*) control samples were prepared and tested in the study. The procedure was performed at the Anschutz Medical Campus at the University of Colorado, Denver. The fixed samples were then transported to the University of Vermont for scanning.

*Micro-CT Scanning*

Micro-CT scans were performed with a Bruker 1173 SkyScan at a voxel resolution of 6 µm at 30 kV/160 µA. Each embedded sample was cut and secured to the scanning pedestal with a thin layer of sticky putty. Cross-sectional images of the entire sample were taken with rotation steps of 0.1 degrees (producing 3600 images). Final reconstructed images comprised 3D matrices of tissue density expressed as Hounsfield units (HU); dimensionless units obtained from the linear transformation of the measured attenuation coefficients [18].

*Three-Dimensional Local Connected Fractal Dimension (3D LCFD)*

Our FA applied a modified version of the box-counting method in conjunction with local connectivity evaluations to calculate the $FD$ of every voxel in each reconstructed image. To reiterate, in the standard box-counting method a square grid of box length $L$ is overlayed on the image and the number of boxes, $N_L$, that cover all elements of the image is counted. The $FD$ is thus defined by the equation

$$FD = \lim_{L \to 0} \frac{\log N(L)}{\log 1/L} \quad (1)$$

In the modified 3D box-counting approach, nested cubes are used in place of 2D concentric squares. For each voxel in the CT image, we take a cubic region $R$ centered at voxel $r$. The region $R$ includes $w$ voxel on each side of $r$. If we let $h = 2w + 1$, which ensures that a center voxel always exists at a step size of two, then $R$ is defined by the cubic subsection of size $h\ x\ h\ x\ h$. We then apply local connectivity and define a new region $R'$, in which voxels in $R$ that are not connected to the center voxel are removed. $R'$ is then subdivided into concentric 3D

boxes centered at $r$ with increasing side lengths $S_L$, where $S_L = \{3, 5, \ldots (h-2), h\}$. Then for each $L$ in the cubic subregions $S_L$ , $N(L)$ in the number of voxels in that neighborhood. The expressions for $L$ and $N(L)$ are then substituted back into equation 1 to calculate the 3D LCFD for each voxel $r$. This approach follows the process illustrated in Figure 2 in three dimensions.

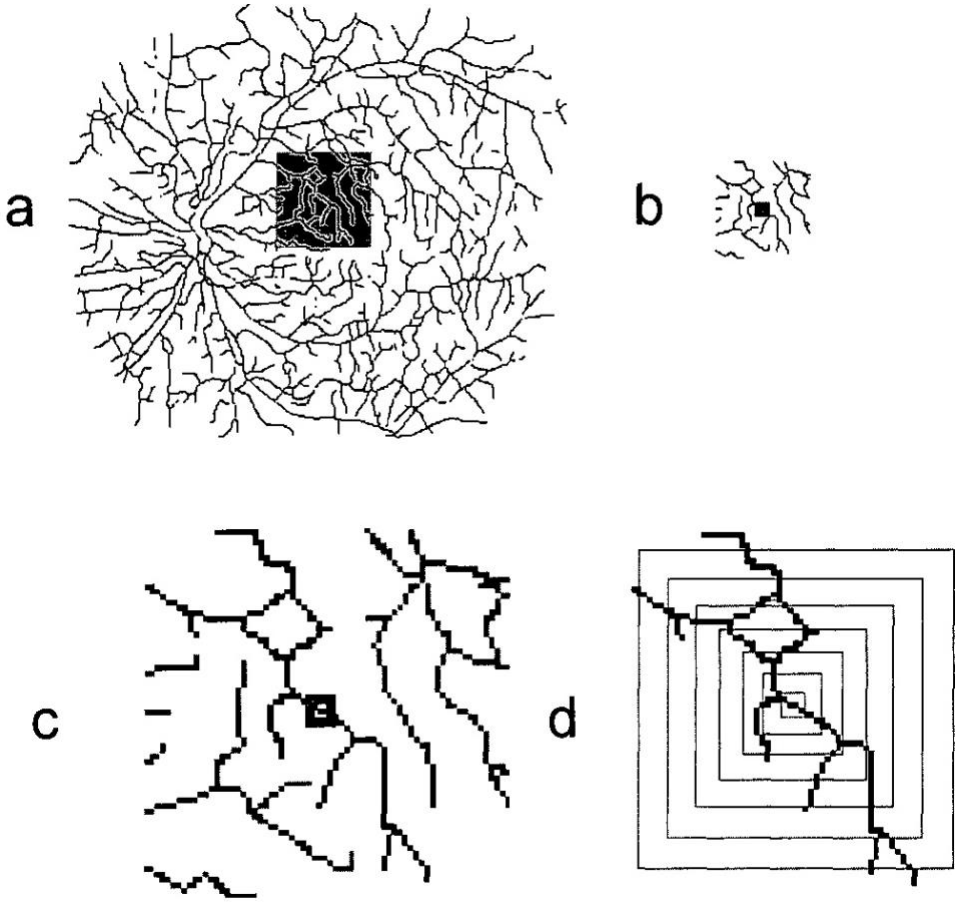


**Figure 2:** Two-dimensional example of the local connected fractal dimension (LCFD). A square subsection of size $h\ x\ h$ is taken from the sample **(a)**, and the center pixel is identified **(b).** The region, which we define as $R$, contains all tissue components **(c)**. Only the components connected to the center pixel are included, and nested boxes of increasing size are overlayed on the image to calculate the FD **(d).** Our approach applies the same concept in three dimensions, using voxels instead of pixels [19].

*3D LCFD Analysis*

3D LCFD calculations were performed using code written in MATLAB R2022b. Digital Imaging and Communications in Medicine (DICOM) files containing the images for each sample were loaded into the MATLAB workspace. Voxel values were converted to HU and then rescaled post -conversion to restore zeroes, corresponding to areas without tissue (airspace). Voxel clusters with fewer than 6 connected components were excluded from the analysis. The maximum side

length of the cubic subregion, h, was set to 17 voxel widths, corresponding to a maximum nested 3D box size of 17 x 17 x 17 centered on voxel $r$. The voxels not connected to $r$ were excluded from the analysis as described in Figure 2. The FD was then calculated using increasing nested 3D boxes of side lengths 3, 5, 7, 9, 11, 13, 15, and 17, respectively, following the 3D LCFD method and equation 1. This process was repeated for every nonzero voxel in the image, producing a list of the FD corresponding to every voxel in the sample. The code was run through the University of Vermont Advanced Computing Core (VACC), a high-performance computing core.

*Visualization*

Micro-CT scans were reconstructed using NRecon reconstruction software. A kernel density estimation (KDE) plot was produced for each sample to compare the distribution of fractal values in each sample, and the mean and median fractal values were calculated. Fractal values over 3 were removed from the dataset before calculating the mean and median fractal values. Arbitrary sections from each plane of the sample (X-Y, X-Z, Y-Z) were taken and conjoined, forming a 3D sliced reconstruction of tissue density behavior in HU. A color map was also added to visualize variations in density throughout the reconstruction. The mean and median tissue densities across the entire image were also calculated for each sample.

*Statistics*

Two-tailed, unpaired T-tests were performed to compare the FD averages and average tissue densities of the control and BLM groups. Statistical significance was taken as $p < 0.05$ for comparing the means of the two groups ($\alpha = 0.05$). Mann-Whitney U-tests were also performed for both mean and median values of FD and tissue densities, with U = 1 indicating statistical significance (equivalent to $\alpha = 0.05$).

**Results**

Results from the code produced a list of FDs and a 3D array of tissue density in HU for each sample. The average FD for the control group (n = 4) ranged from 2.7755 to 2.8296, with a cumulative average FD of 2.8133 as shown in Table 1. The average FD for the BLM group (n = 5) ranged from 2.8168 to 2.8384, with a cumulative average FD of 2.8276. A t-test and Mann-Whitney U-test revealed no statistical significance between the average fractal values of the two groups. For $\alpha = 0.05$ ($p = 0.275$; U = 5). KDE plots show slightly skewed distributions and so the median FD was also calculated for each sample to better reflect the central tendency of the values. The median FD for the control group ranged from 2.7758 to 2.8353, with an average median value of 2.8172. The median FD for the BLM group ranged from 2.8321 to 2.8509, with an average median value of 2.8397 (Table 1). A Mann-Whitney U-test was performed on the two groups with U = 3, similar to a p-value of ~ 0.15.

**Table 1:** Mean and median FD for BLM and control (CTRL) groups. Cumulative averages are indicated in the last line.

| | BLM Mean FD | CTRL Mean FD | BLM Median FD | CTRL Median FD |
|---|---|---|---|---|
| Animal 1 | 2.8168 | 2.7755 | 2.8321 | 2.7758 |
| Animal 2 | 2.8217 | 2.8189 | 2.8352 | 2.8238 |
| Animal 3 | 2.83 | 2.8293 | 2.8374 | 2.834 |
| Animal 4 | 2.8312 | 2.8296 | 2.8428 | 2.8353 |
| Animal 5 | 2.8384 | - | 2.8509 | - |
| **Cumulative Average** | **2.8276** | **2.8133** | **2.8397** | **2.8172** |

The average tissue density for the control group ranged from 1,546 to 2,369 HU, with a cumulative average density of 2,057 HU as shown in Table 2. The average tissue density for the BLM group ranged from 1,988 to 6,117 HU, with a cumulative average tissue density of 3,762 HU. There was no statistical significance between the average tissue densities of the two groups for $\alpha$ = 0.05 (p = 0.105, U = 4). The median tissue densities for each group were calculated given the supposition that the distribution of tissue density could also be skewed. The median tissue density ranged from 1,361 to 1,979 HU for the control group and 1,688 to 6,032 HU for the BLM group. The average median tissue density of the control and BLM samples was 1,677 HU and 3,511 HU, respectively. A Mann-Whitney U-test was performed with U = 3 (p ~ 0.15), indicating no statistically significant result for $\alpha$ = 0.05.

**Table 2:** Mean and median tissue density for BLM and control groups. Cumulative averages are indicated in the last line.

| | BLM Mean Tissue Density (HU) | CTRL Mean Tissue Density (HU) | BLM Median Tissue Density (HU) | CTRL Median Tissue Density (HU) |
|---|---|---|---|---|
| Animal 1 | 1988 | 1546 | 1688 | 1361 |
| Animal 2 | 2103 | 1973 | 1892 | 1513 |
| Animal 3 | 3767 | 2339 | 3339 | 1856 |
| Animal 4 | 4834 | 2369 | 4604 | 1979 |
| Animal 5 | 6117 | | 6032 | |
| **Cumulative Average** | **3762** | **2057** | **3511** | **1677** |

*KDE Plots and 3D Sliced Reconstructions*

FD values between 0 and 3 were included in the KDE plots. All samples display a left-skewed distribution in KDE plots for the allowed FD range except for CTRL2B, which is left-shifted relative to the other samples and has a more normal FD distribution (Figure 5). Sample CTRL2B also has the lowest mean and median FD of 2.7755 and 2.7758, respectively. The 3D sliced reconstruction of CTRL2B illustrates a fairly homogeneous tissue density structure with higher concentrations surrounding airways (Figure 6). In the BLM sample, a similar architecture is seen, however, there is also thickening around the periphery of the lungs indicated by a shift in color associated with greater HU (Figure 8). Other 3D sliced reconstructions do not capture the periphery of the lungs as well as in Figure 8 but can be found in the supplementary material along with the remaining KDE plots.

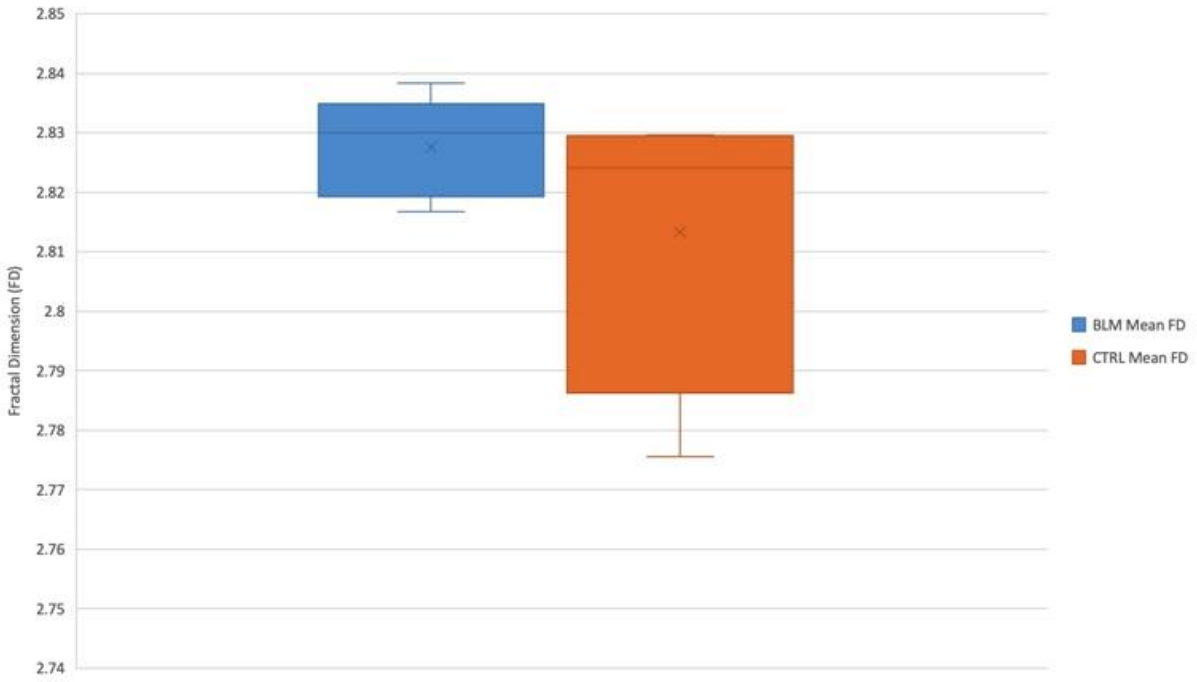


**Figure 3:** Box and whisker plot of the mean FD for BLM and control samples.

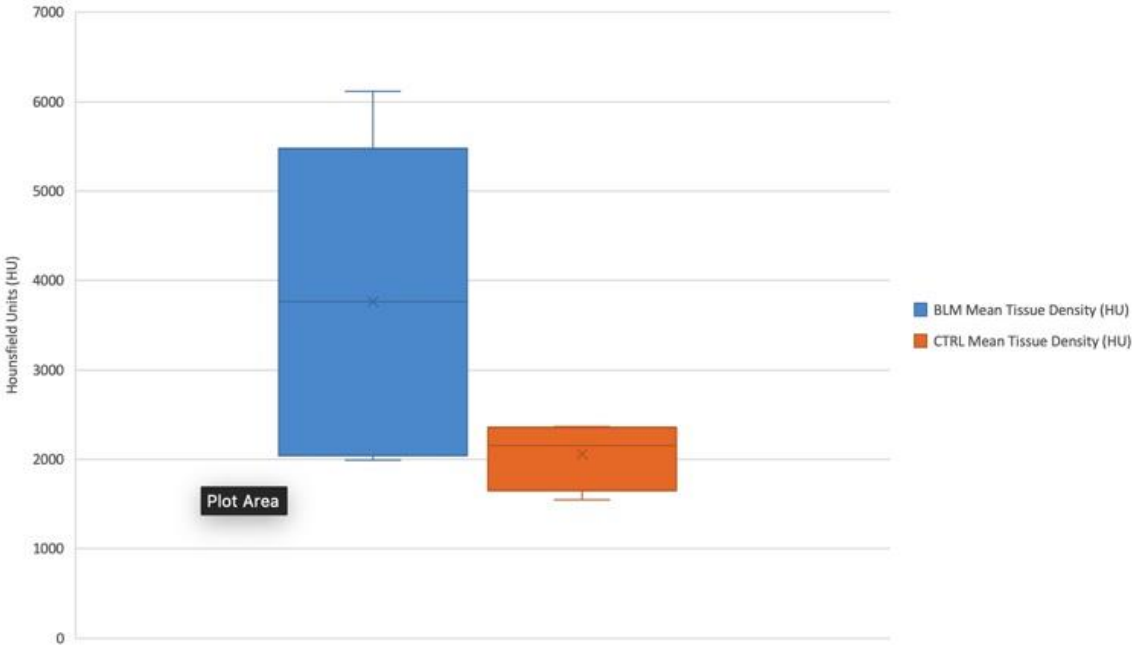


**Figure 4:** Box and whisker plot of the mean tissue density (HU) for BLM and control samples.

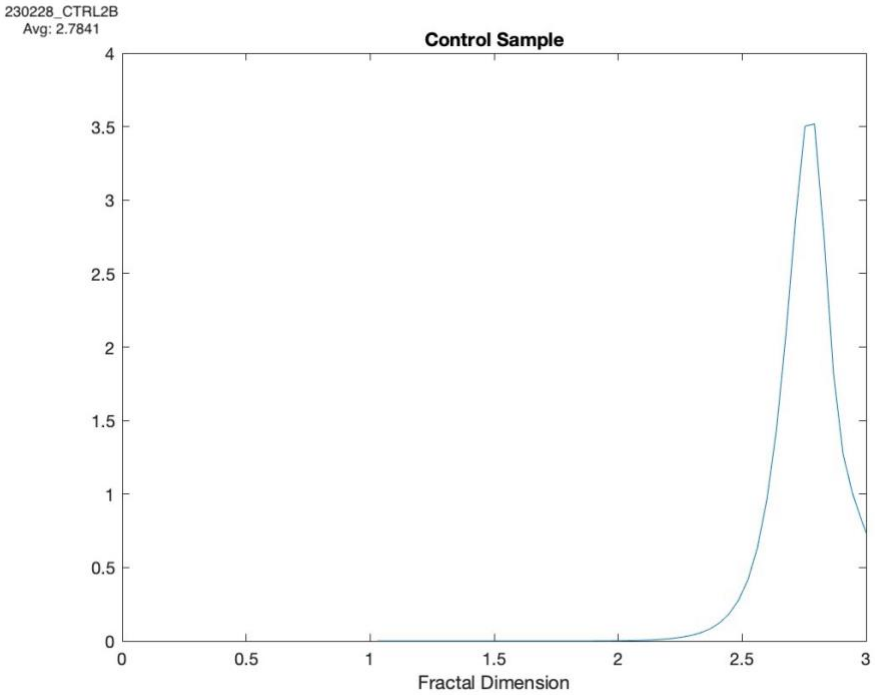


**Figure 5:** Kernel Density Estimation (KDE) plot displaying the distribution of fractal values of control sample CTRL2B.

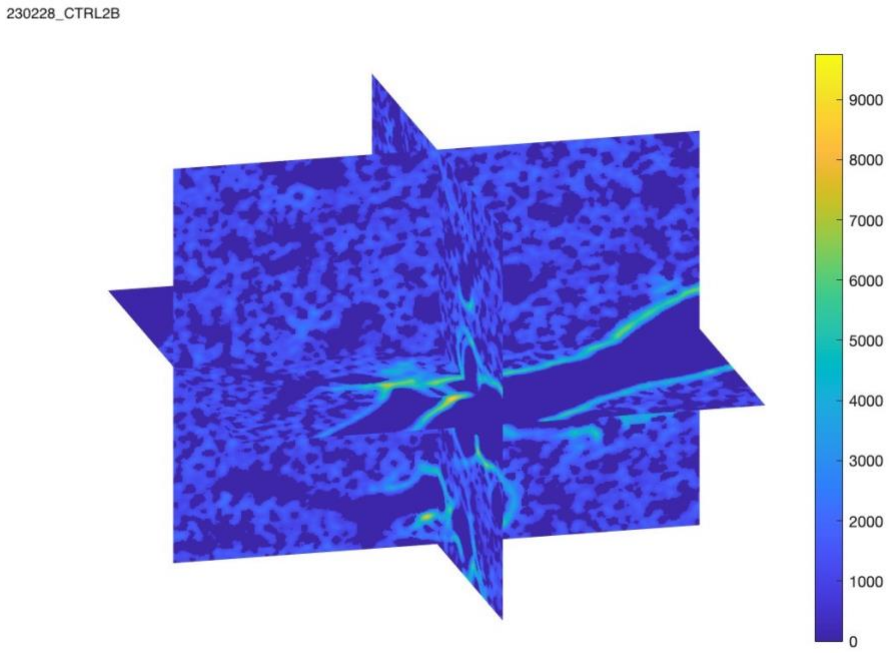


**Figure 6:** 3D sliced reconstruction of control sample CTRL2B. A color bar is added on the right, representing tissue density in Hounsfield units. Higher-density tissue can be seen surrounding the airways.

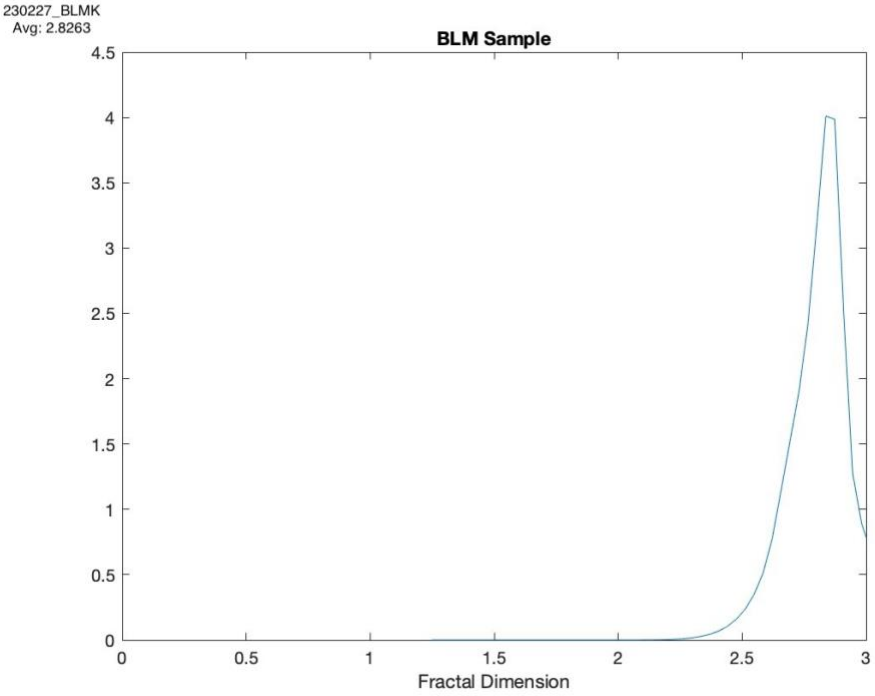


**Figure 7:** Kernel Density Estimation (KDE) plot displaying the distribution of fractal values of BLM sample BLMK.

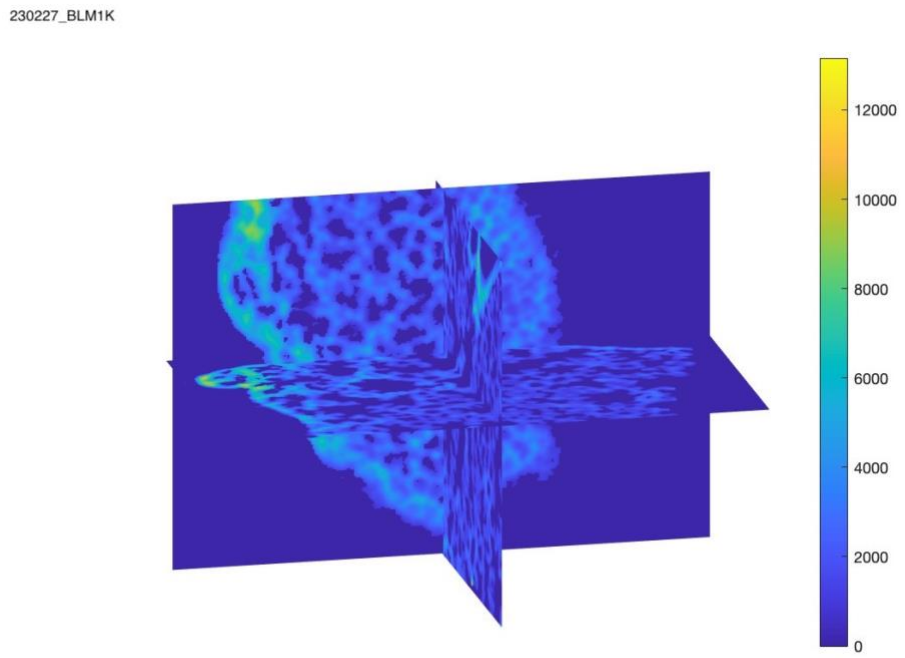


**Figure 8:** 3D sliced reconstruction of BLM sample BLM1K. A color bar is added on the right, representing tissue density in Hounsfield units. Greater tissue density is observed on the lung periphery, a consistent structural characteristic of IPF.

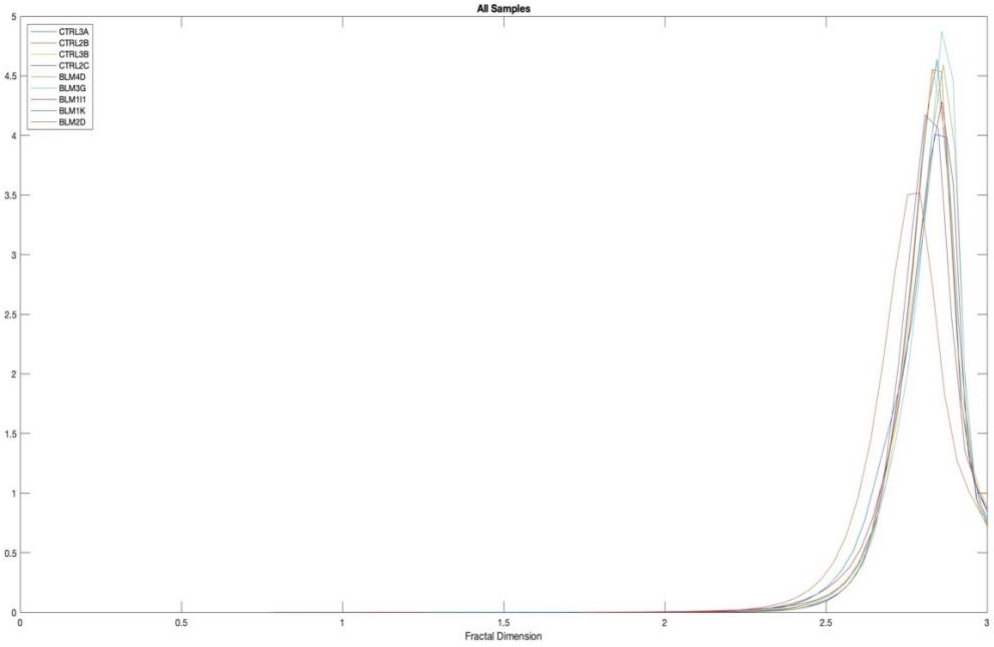


**Figure 9:** Kernel Density Estimation (KDE) plot of the FD distribution for all samples (n = 4 control; n = 5 BLM). Distributions shifted to the right correspond with higher tissue connectedness.

**Discussion**

In this work, a three-dimensional fractal analysis was applied to characterize the structure of lung tissue as opposed to traditional 2D methods, as it provides a more complete measure of tissue heterogeneity. Local connectivity was also integrated into the analysis as it better reflects spatial variation, producing a distribution of LCFDs for each region rather than a single measurement of the tissue as a whole. A modified 3D box-counting method was applied across every voxel in the sample image to produce a range of fractal values, which, combined with local connectivity, can be used to investigate and compare particular areas of interest within the lung (such as the periphery). A distribution of FDs also allows us to perform statistical analyses for more complete comparisons. It also allows us to visualize tissue complexities through KDE plots and 3D sliced reconstructions, both of which present quantifiable data on the arrangement of lung tissue. In this approach, we can better examine the structural behavior of fibrosis in healthy and diseased lungs by accounting for collagen thickness and connectivity.

Although a sample size of 4 control and 5 BLM lungs is not sufficient to make any statistical conclusions concerning the FDs and tissue densities, the data do indicate a subtle distinction between groups in which BLM samples exhibit a greater cumulative average tissue density and FD. When comparing control and BLM groups, no statistical significance was found in any of the T-tests or Mann-Whitney U-tests for $\alpha$ = 0.05 and U = 1, respectively. However, relatively low p and U values were produced, especially for mean and median tissue density comparisons (p = 0.105; U = 3). This indicates that there is an emerging disparity between groups, even with only nine samples to compare. It is expected that the addition of more samples will enhance this disparity by lowering the variance of the mean and median FDs and tissue densities, but this cannot be confirmed without further testing.

Visually, the difference in tissue density and collagen distribution between groups is more marked in some samples. This is because sections extracted for 3D sliced reconstructions are taken arbitrarily, resulting in different regional comparisons. For instance, the 3D sliced reconstruction of BLM1K successfully captures the lung periphery and indicates a higher relative tissue density, a pattern consistent with UIP and fibrotic development in IPF (Figure 8). However, this region is not captured in many of the other samples, making it hard to determine if the tissue behavior seen in BLM1K is (Figure 6). Processing and array size limitations in MATLAB prevent entire samples from being shown. However, imaging more slice locations may help to compare specific regions of the lungs. A common feature seen in all samples is the presence of higher tissue densities surrounding the airways. This presents a limitation, as FD distributions are influenced by the number of airways in each sample. Fibrotic airways are not a distinguishing feature of IPF and may therefore skew the results by presenting indications of IPF when there are none.

The results of the box and whisker plots (Figures 3 and 4) indicate that BLM samples have a greater range of tissue densities but a smaller degree of variability in average FD values compared to the control samples. The 3D LCFD analysis proposed in this study does not account for tissue density, as the two analyses are performed separately. The results of the tissue

density comparisons have the strongest indication of statistically significant findings. Therefore, it may be useful to incorporate tissue density into the fractal analysis considering that collagen content is a significant factor in IPF development. This methodology would entail a four-dimensional (4D) characterization of lung tissue, calculating the FD of every voxel in the sample like before but with density-based weighting (the "$4^{th}$" dimension). This approach would also determine if tissue density affects the distribution of FDs (KDE plot behavior) and the average FD value.

Control sample CTRL2B exhibits a slightly more normal distribution and lower average FD. A normal distribution is likely attributed to greater tissue homogeneity, which is expected in healthy lungs. In contrast, a skewed distribution is indicative of tissue heterogeneity. In particular, a right-shifted and/or left-skewed distribution is associated with increased tissue connectedness, indicated by greater local voxel connectivity defined by our 3D LCFD analysis approach. Anatomically, this is due to increased tissue concentration (density) and/or collagen remodeling, which are hallmark characteristics of IPF. In other words, KDE distribution shifts and the concomitant increase in tissue connectedness could be caused by a combination of increased collagen deposition and/or reorganization of the existing collagen. This is the case with honeycombing.

The relative extent to which the skewed and/or shifted distributions are caused by increased tissue density can be observed by applying the suggested 4D LCFD. Interestingly, the median tissue densities for all samples are lower than the mean tissue densities, signifying a left-skewed tissue density distribution. However, the skewness of the FD distributions does not reflect this and varies regardless of whether in the BLM or control group. This may be due to normalization features in the code and/or artifacts in the micro-CT images (Figure 10) and presents another motivation for employing a density-inclusive 4D LCFD analysis. While excluded in the analysis, the large quantity of FD values above 3 present in each sample necessitates a closer look at the code, as we expect values exclusively in the range of 0 to 3. FD distributions are also likely influenced by increased collagen content surrounding airways as mentioned previously. The image resolution is also limited to the scanning capabilities of the Bruker 1173 SkyScan and may fail to capture much of the fractal nature of the lung tissue with the settings used in this study. A voxel resolution closer to ~1 μm may be required to capture the alveolar airspaces of the lungs.

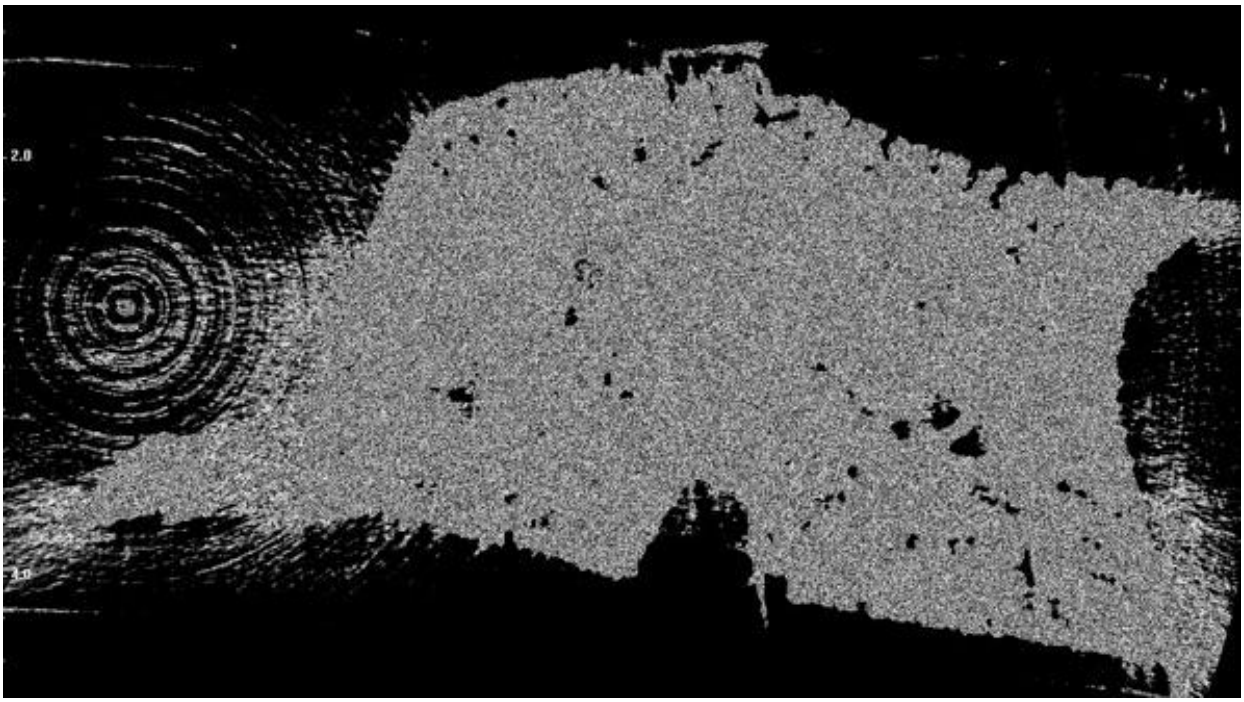

**Figure 10:** Single micro-CT image of sample CTRL2C with a ring artifact. While MATLAB code was written to exclusively capture giant components, elements from the artifact may have impacted 3D LCFD analysis and results.

*Future Investigations*

Among the limitations of the study are the small number of samples tested. Therefore, more samples should be tested using the same 3D LCFD analysis outlined in this study to reduce the variance in the control and BLM samples. The results reveal emerging disparities between the tissue densities and FDs of the two groups, however, statistical significance has not been confirmed for the given sample size. Future works applying a 4D LCFD analysis may better characterize lung tissue architecture by incorporating density into the calculation, thereby accounting for both collagen connectivity and concentration rather than connectivity alone. Normalized tissue density in HU would provide the $4^{th}$ dimension by assigning each voxel a weighted value in this newly suggested approach. The 3D LCFD method in its current or newly proposed form can be applied to other diseases of the lungs, such as emphysema, and other regions of the body. It is difficult to scale the approach to full reconstructions of the human lungs or other entire organs due to limited computing capabilities, however, small sections may be analyzed. This analysis could therefore be suitable for comparing a small section of the periphery in healthy and diseased, or potentially diseased lungs.

**Conclusion**

The 3D LCFD analysis proposed in this study successfully produced an FD distribution for control and BLM samples mimicking IPF. Although no statistical significance was found between the

two groups for $\alpha$ = 0.05 and U = 1, there were numerical and visual disparities in the FD and tissue density means and medians, indicating structural remodeling and/or increased collagen concentration in BLM samples. These are only emerging assumptions given the small sample sizes; however, we predict that including more samples in the study will reduce the variance and reveal more concrete and statistically significant differences between the two groups. Factoring in density into the fractal analysis may better capture the lung architecture and should be implemented in future trials. Ultimately, this model provides a basis for a 3D and even 4D fractal analysis of lung structure in IPF, with potential applications in clinical diagnostics, prognostics, and other disease progression and presentation analysis.

**Acknowledgments**

This work is supported by Anschutz Medical Campus at the University of Colorado and the Robert Larner, M.D. College of Medicine at the University of Vermont, and would not have been possible without the supervision of Jason H.T. Bates Ph.D., D.Sc. Coding, editing, and statistical analyses were performed with help from Dylan T. Casey, Vitor Mori, and Cameron Lunn, as well as the University of Vermont Advanced Computing Core.

**Conflicts of Interest**

The author declares no conflicts of interest.

**References**

[1] F. J. Martinez *et al.*, "Idiopathic pulmonary fibrosis," *Nat Rev Dis Primers*, vol. 3, no. 1, Art. no. 1, Oct. 2017, doi: 10.1038/nrdp.2017.74.

[2] N. Hoyer, T. S. Prior, E. Bendstrup, T. Wilcke, and S. B. Shaker, "Risk factors for diagnostic delay in idiopathic pulmonary fibrosis," *Respir Res*, vol. 20, p. 103, 2019, doi: 10.1186/s12931-019-1076-0.

[3] A. L. Association, "Pulmonary Fibrosis Medications." https://www.lung.org/lung-health-diseases/lung-disease-lookup/pulmonary-fibrosis/patients/how-is-pulmonary-fibrosis-treated/medications (accessed Apr. 27, 2023).

[4] H. Fujimoto, T. Kobayashi, and A. Azuma, "Idiopathic Pulmonary Fibrosis: Treatment and Prognosis," *Clin Med Insights Circ Respir Pulm Med*, vol. 9, no. Suppl 1, pp. 179–185, Dec. 2016, doi: 10.4137/CCRPM.S23321.

[5] J. Sauleda, B. Núñez, E. Sala, and J. B. Soriano, "Idiopathic Pulmonary Fibrosis: Epidemiology, Natural History, Phenotypes," *Med Sci (Basel)*, vol. 6, no. 4, p. 110, Nov. 2018, doi: 10.3390/medsci6040110.

[6] "Emerging therapies for idiopathic pulmonary fibrosis, a progressive age-related disease | Nature Reviews Drug Discovery." https://www.nature.com/articles/nrd.2017.170 (accessed Apr. 27, 2023).

[7] J. Herrera, C. A. Henke, and P. B. Bitterman, “Extracellular matrix as a driver of progressive fibrosis,” *J Clin Invest*, vol. 128, no. 1, pp. 45–53, doi: 10.1172/JCI93557.
[8] G. Raghu *et al.*, “Diagnosis of Idiopathic Pulmonary Fibrosis. An Official ATS/ERS/JRS/ALAT Clinical Practice Guideline,” *Am J Respir Crit Care Med*, vol. 198, no. 5, pp. e44–e68, Sep. 2018, doi: 10.1164/rccm.201807-1255ST.
[9] “Fractals and Complexity.” https://imagej.nih.gov/ij/plugins/fraclac/FLHelp/Fractals.htm (accessed Apr. 27, 2023).
[10] N. Tanabe, S. Sato, B. Suki, and T. Hirai, “Fractal Analysis of Lung Structure in Chronic Obstructive Pulmonary Disease,” *Front Physiol*, vol. 11, p. 603197, Dec. 2020, doi: 10.3389/fphys.2020.603197.
[11] M. G. Jones *et al.*, “Three-dimensional characterization of fibroblast foci in idiopathic pulmonary fibrosis,” *JCI Insight*, vol. 1, no. 5, p. e86375, doi: 10.1172/jci.insight.86375.
[12] S. Krohn *et al.*, “Evaluation of the 3D fractal dimension as a marker of structural brain complexity in multiple-acquisition MRI,” *Hum Brain Mapp*, vol. 40, no. 11, pp. 3299–3320, May 2019, doi: 10.1002/hbm.24599.
[13] J. Piera, V. Parisi-Baradad, E. García-Ladona, A. Lombarte, L. Recasens, and J. Cabestany, “Otolith shape feature extraction oriented to automatic classification with open distributed data,” *Marine and Freshwater Research - MAR FRESHWATER RES*, vol. 56, Jan. 2005, doi: 10.1071/MF04163.
[14] J. Tashiro *et al.*, “Exploring Animal Models That Resemble Idiopathic Pulmonary Fibrosis,” *Front Med (Lausanne)*, vol. 4, p. 118, Jul. 2017, doi: 10.3389/fmed.2017.00118.
[15] S. W. Aesif *et al.*, “In Situ Analysis of Protein S-Glutathionylation in Lung Tissue Using Glutaredoxin-1-Catalyzed Cysteine Derivatization,” *Am J Pathol*, vol. 175, no. 1, pp. 36–45, Jul. 2009, doi: 10.2353/ajpath.2009.080736.
[16] V. Anathy *et al.*, “Oxidative Processing of Latent Fas in the Endoplasmic Reticulum Controls the Strength of Apoptosis,” *Mol Cell Biol*, vol. 32, no. 17, pp. 3464–3478, Sep. 2012, doi: 10.1128/MCB.00125-12.
[17] T. Wellman, J. Mondoñedo, G. Davis, J. Bates, and B. Suki, “Topographic distribution of idiopathic pulmonary fibrosis: A hybrid physics- and agent-based model,” *Physiological Measurement*, vol. 39, Jun. 2018, doi: 10.1088/1361-6579/aaca86.
[18] K. Greenway, “Hounsfield unit | Radiology Reference Article | Radiopaedia.org,” *Radiopaedia*. https://radiopaedia.org/articles/hounsfield-unit?lang=us (accessed Apr. 27, 2023).
[19] G. Landini, P. Murray, and G. P. Missonf, “Local Connected Fractal Dimensions and Lacunarity Analyses of 60 ° Fluorescein Angiograms,” 2005. Accessed: Apr. 27, 2023. [Online]. Available: https://www.semanticscholar.org/paper/Local-Connected-Fractal-Dimensions-and-Lacunarity-%C2%B0-Landini-Murray/672487eac077c29af5f3715eddeed09165ac2925

## Supplementary Material

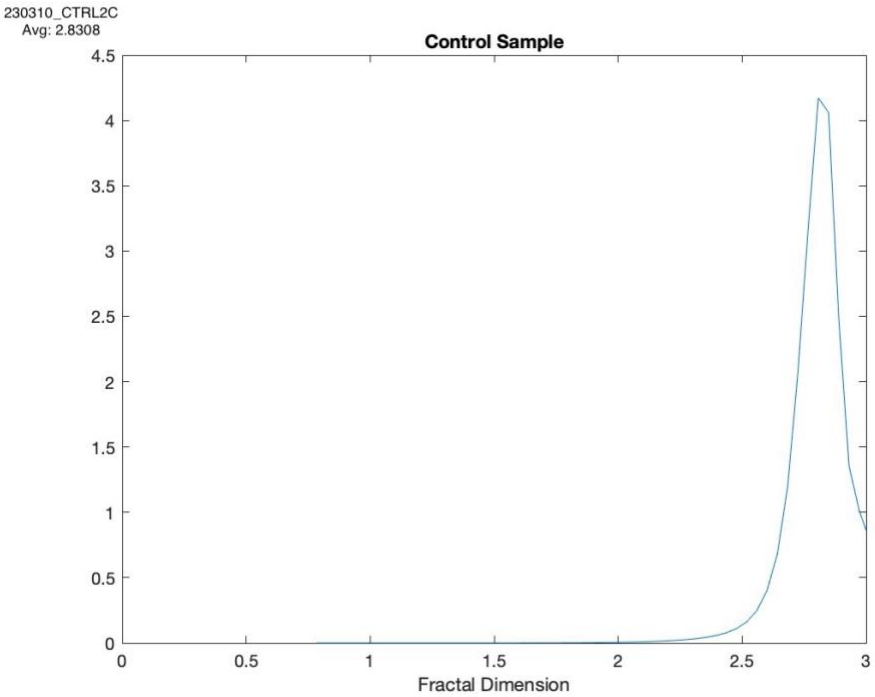


**Figure 11:** KDE plot of control sample CTRL2C.

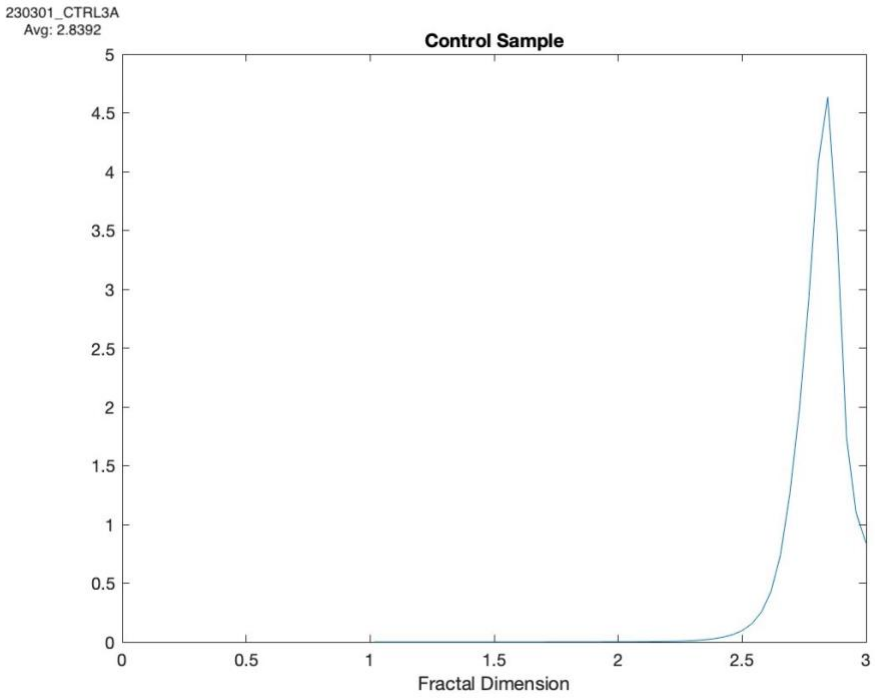


**Figure 12:** KDE plot of control sample CTRL3A.

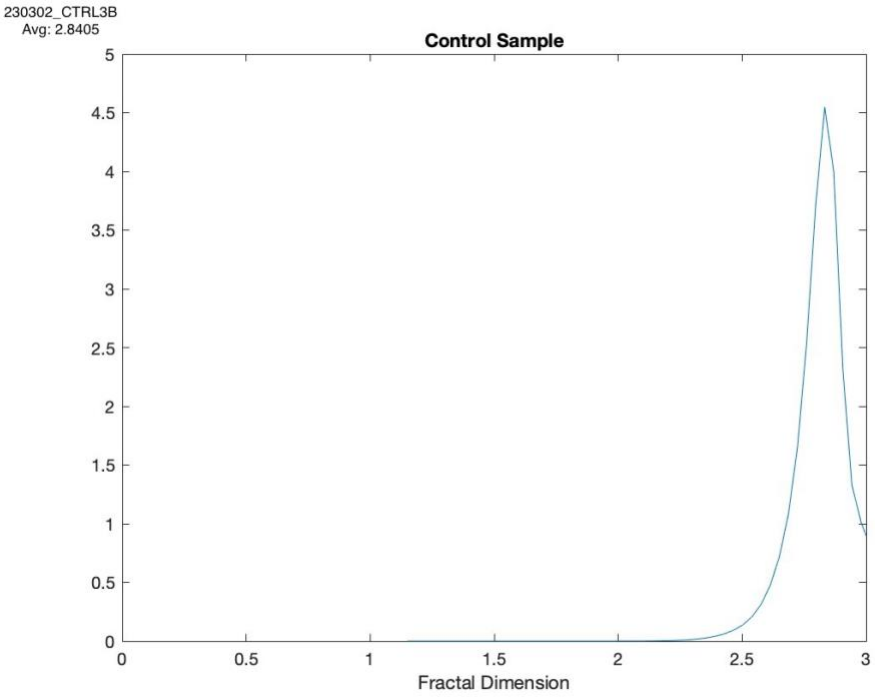


**Figure 13:** KDE plot of control sample CTRL3B.

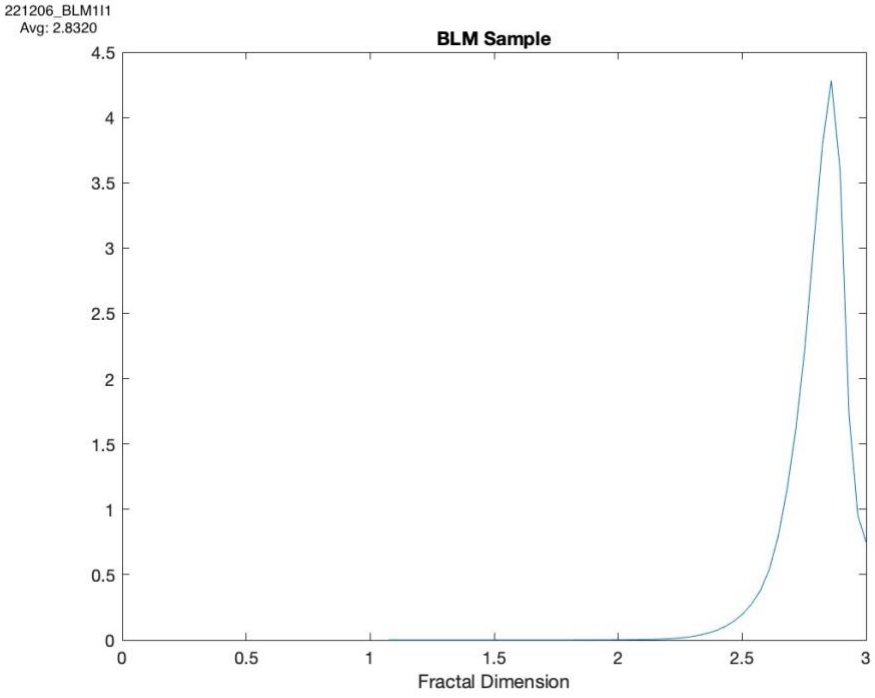


**Figure 14:** KDE plot of BLM sample BLM1I1.

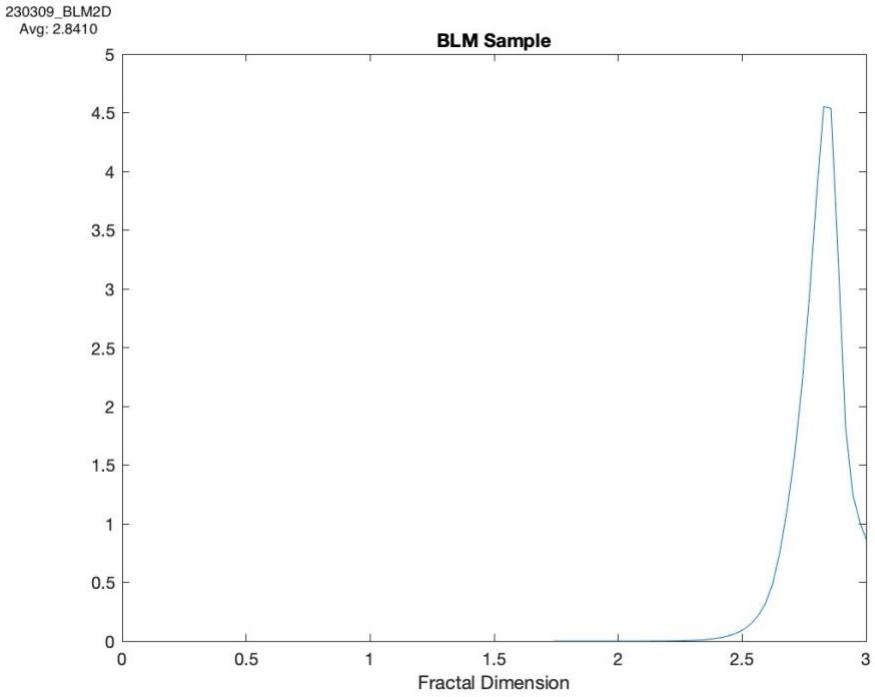


**Figure 15:** KDE plot of BLM sample BLM2D.

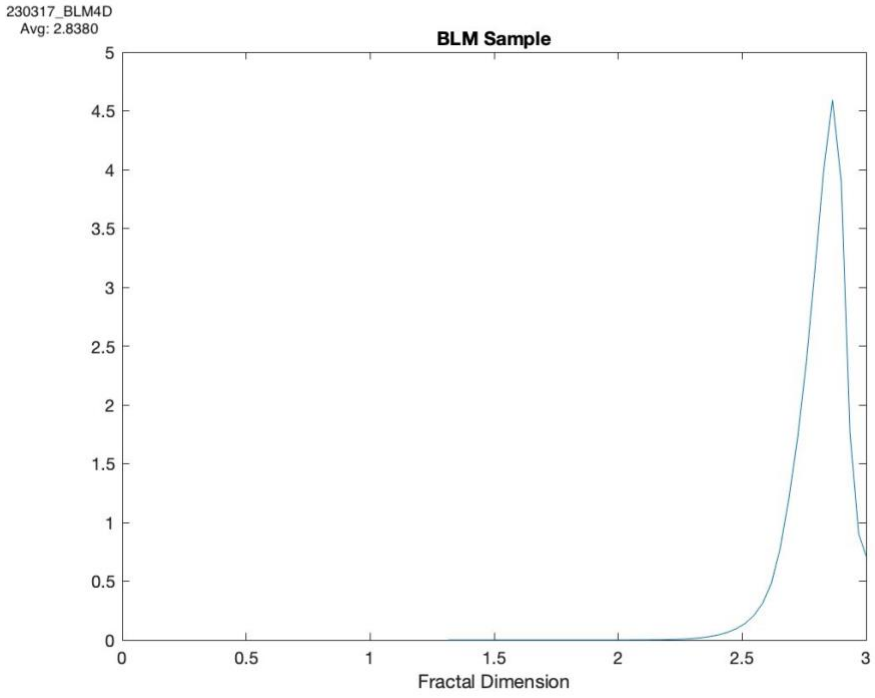


**Figure 16:** KDE plot of BLM sample BLM4D.

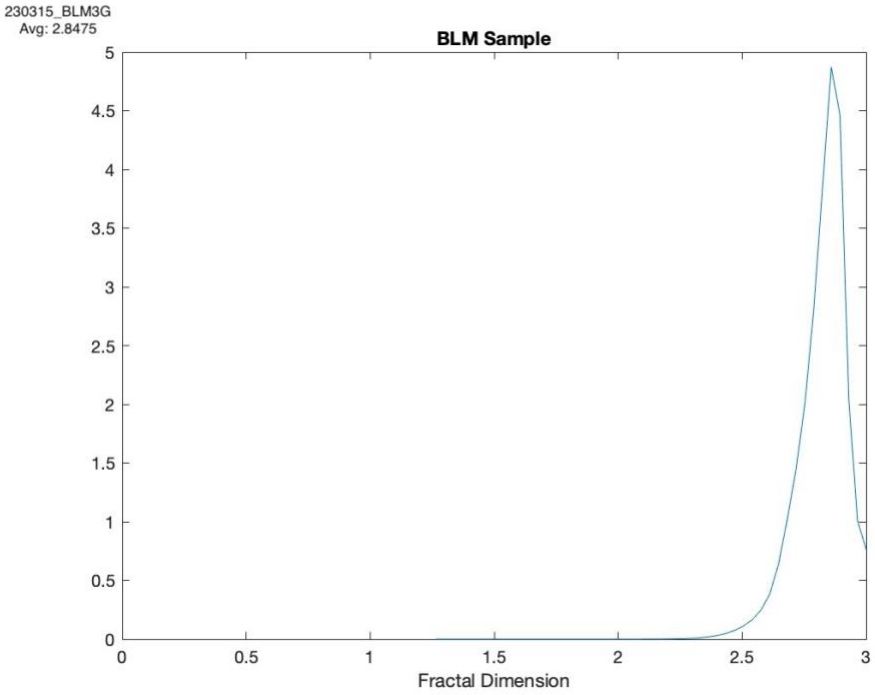


**Figure 17:** KDE plot of BLM sample BLM3G.

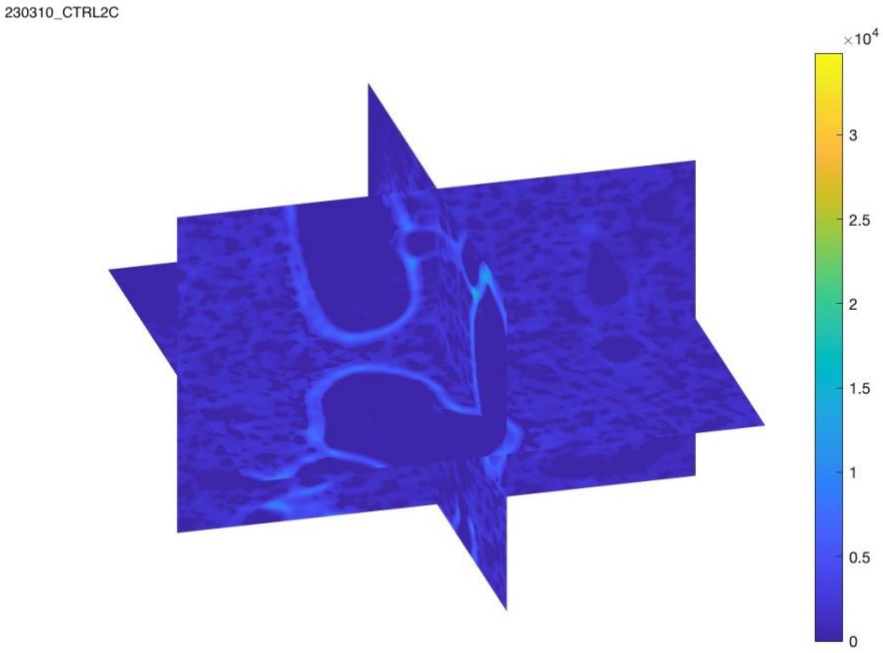


**Figure 18:** 3D sliced reconstruction of control sample CTRL2C.

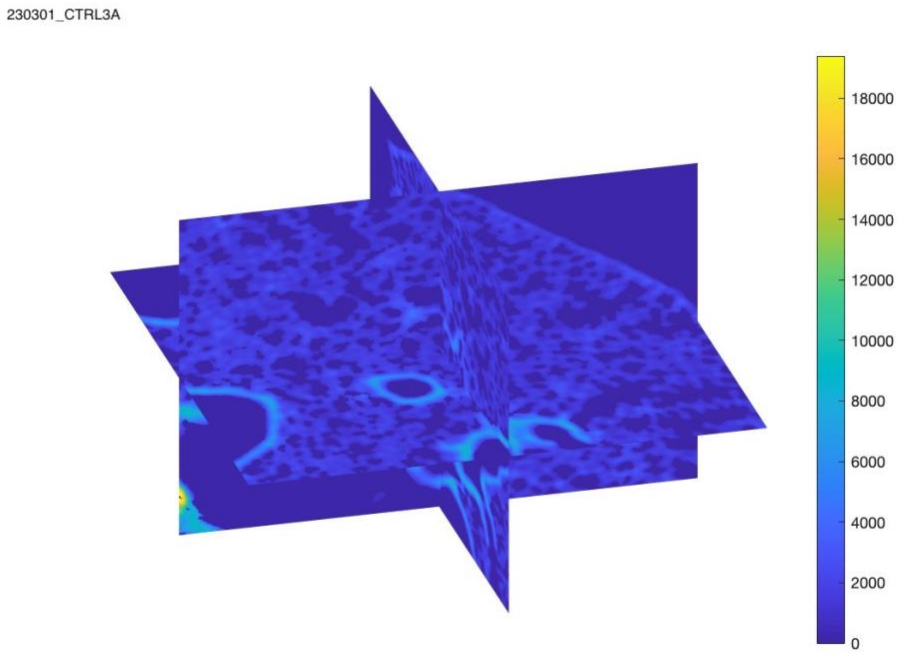


**Figure 19:** 3D sliced reconstruction of control sample CTRL3A.

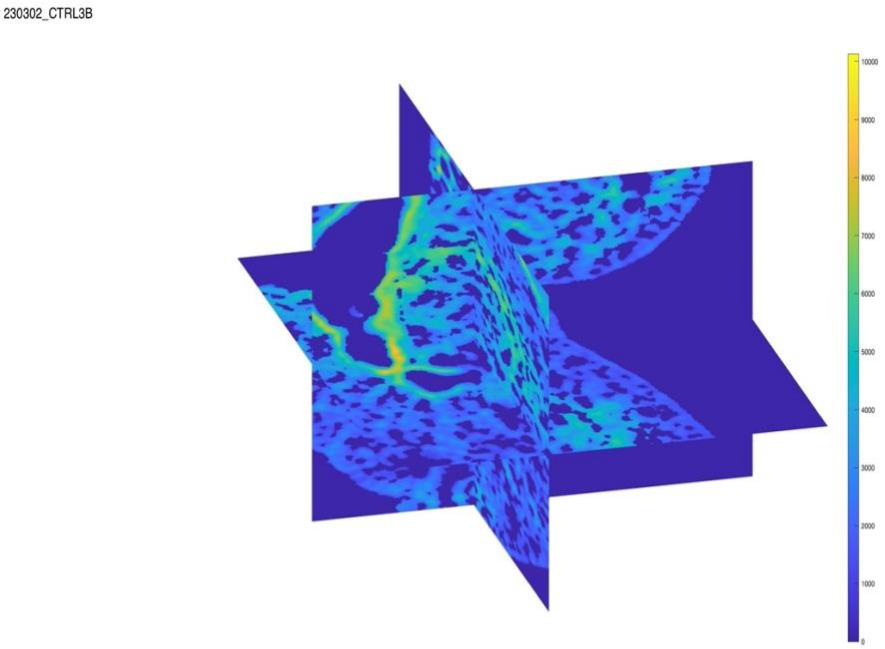


**Figure 20:** 3D sliced reconstruction of control sample CTRL3B.

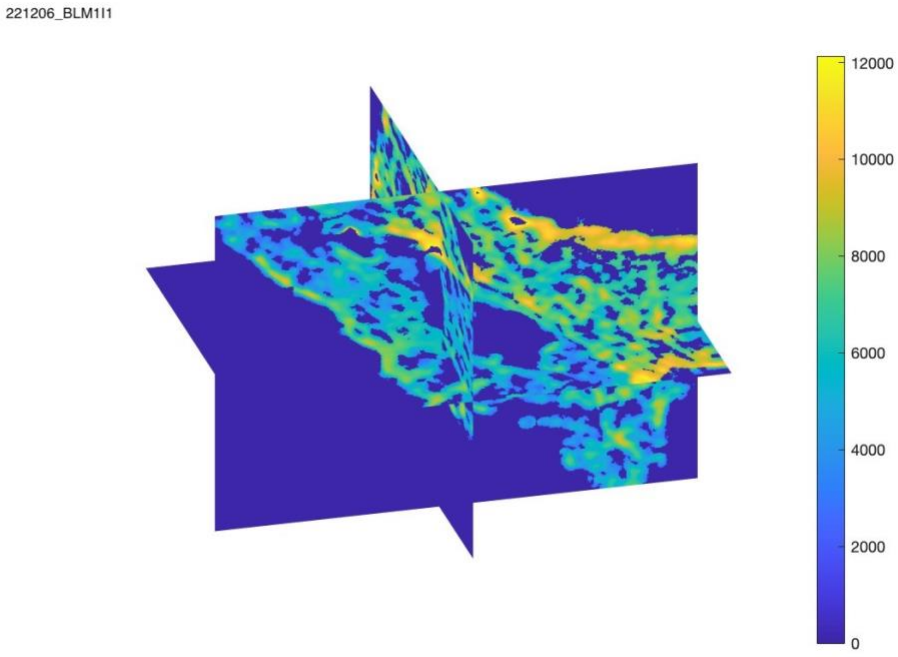


**Figure 21:** 3D sliced reconstruction of BLM sample BLM1I1.

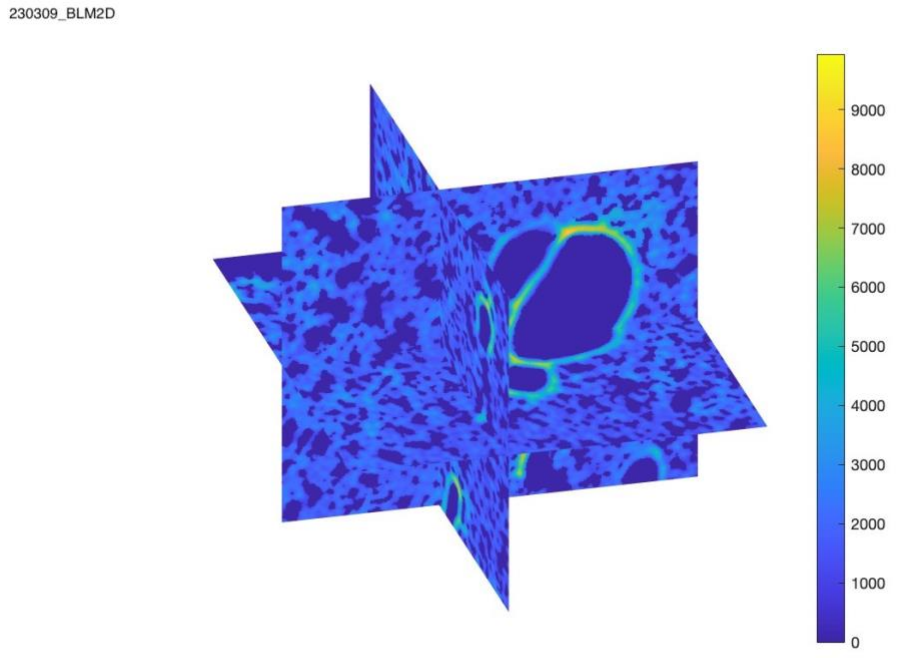


**Figure 22:** 3D sliced reconstruction of BLM sample BLM2D.

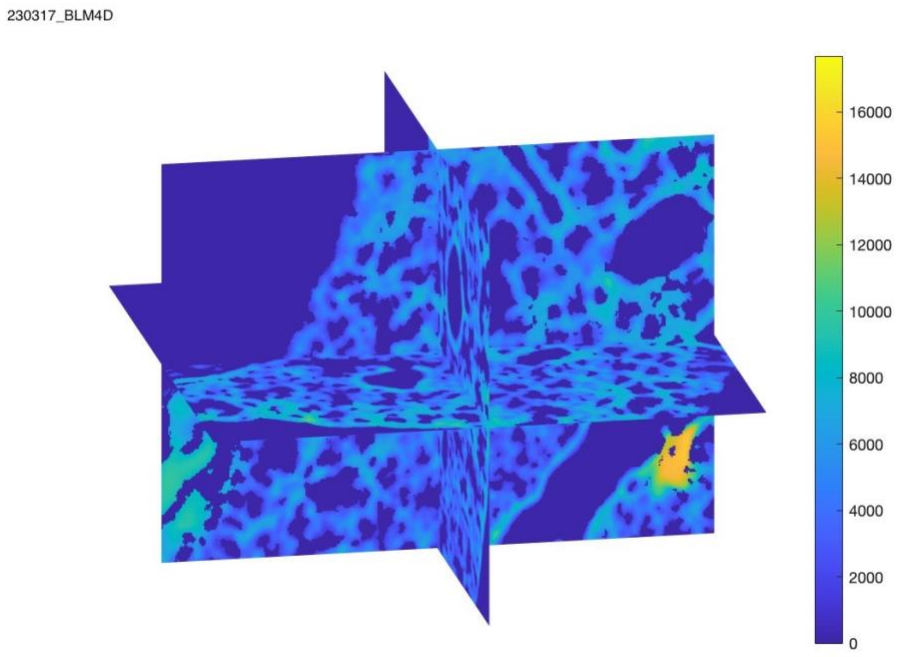


**Figure 23:** 3D sliced reconstruction of BLM sample BLM4D.

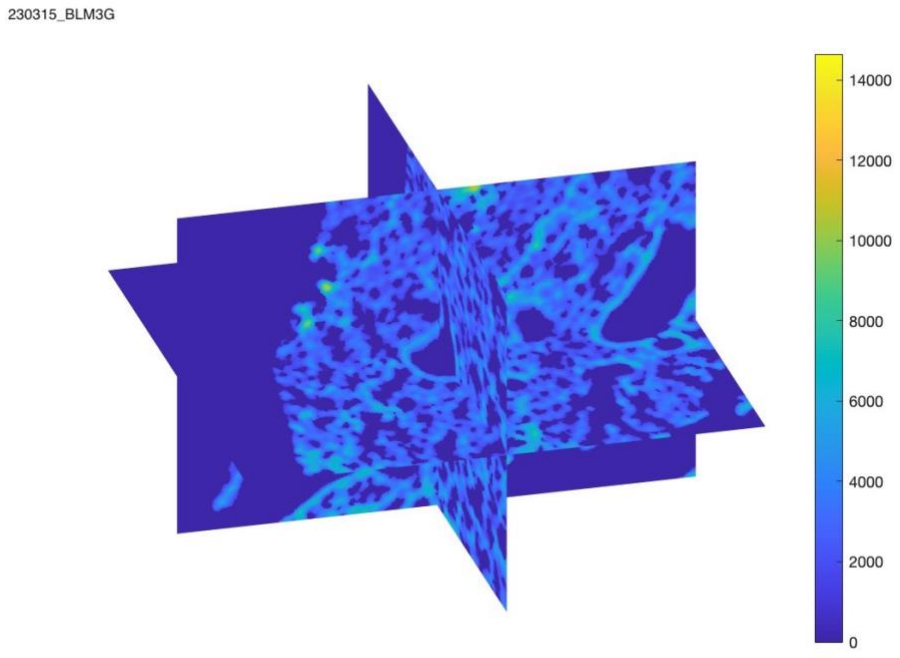


**Figure 24:** 3D sliced reconstruction of BLM sample BLM3G.